Rolling Rod Electrostatic Microgenerator

Michail E. Kiziroglou, *Member, IEEE*, Cairan He, and Eric M. Yeatman, *Senior Member, IEEE*

***Abstract*—The difficulty of maximizing the proof mass, and lack of broadband operation, are key issues for miniaturized energy-harvesting devices. Here, a novel electrostatic energy harvester is presented, employing an external free-rolling proof mass to address these issues. A description of the operating principle is given, and the kinetic dynamics of the cylinder are analyzed. The electrostatics of the system are simulated, identifying the device performance for different dielectric dimensions and surface specifications. The fabrication of a prototype device is presented, and physical characterization results demonstrate a successful fabrication technique for dielectric sizes down to 100 nm. Capacitance measurements reveal a capacitance ratio of 4 and are in agreement with simulation results. A voltage gain of 2.4 is demonstrated. The device is suitable for energy harvesting from low-frequency high-amplitude ambient motion sources such as the human body.**

***Index Terms*—Electrostatic, energy harvesting, microelectromechanical systems (MEMS), power scavenging.**

I. Introduction

ENERGY-harvesting devices are attractive for applications where battery replacement is impractical, either because of position inaccessibility, a large number of devices, or both. Such applications include body-mounted medical sensors and implantable devices, wireless sensor networks, structural and field condition monitoring, and sensors in vehicle tires. In many of these cases, light is not reliably available, and temperature gradients are modest, making ambient motion a more suitable source of power.

The low frequencies of body motion offer limited power densities [1], and since a high degree of miniaturization is desirable, achieving near-optimal designs will be necessary for these applications to be feasible. A wide range of motion-scavenging devices has been reported [2]; most are based on a proof mass mounted on a frame with a flexible suspension, with power generated by damping the relative proof mass motion with a transducer element.

While electromagnetic forces are most suitable for energy conversion at macroscopic dimensions, scaling laws make electrostatic forces more feasible for energy conversion at the millimeter scale and below [3]. Electrostatic devices are also convenient for integrated manufacturing as they do not require the specialized materials and associated fabrication processes of magnetic and piezoelectric systems. For these reasons, electrostatic transduction has been investigated by a number of groups for use in miniature energy-harvesting devices, particularly those implemented in silicon microelectromechanical systems (MEMS).

The first reports were by Meninger *et al.* [4], which describe a monolithic MEMS device with a laterally moving proof mass and comb drive electrostatic transducers. The relative merits of constant charge and constant voltage operation were analyzed. However, successful net power generation from these devices was not reported. Similar devices were also investigated by Roundy *et al.* [5], who also provide the first report of electrostatic harvesters with integrated output electronics. Generally, electrostatic devices have the disadvantage that a precharge or priming voltage must be applied on each cycle, but this can be avoided with the use of integrated electrets. Such electret-based harvesters have been reported by Sterken *et al.* [6].

Successful operation of a nonresonant MEMS device suitable for low-frequency applications, such as body motion, has been reported by Miao *et al.* [7]. More recently, Yen and Lang have reported net power of 1.8 μW from an electrostatic device that incorporates an inductive energy flyback circuit to provide the priming energy [8].

In general, MEMS electrostatic energy harvesters have an integrated mass forming one element of a variable capacitor, with power derived from an electrostatic force between the moving mass and the frame [9]. Such a monolithic device is attractive for size and (potentially) cost reasons, but it has several important limitations. First, maximizing the proof mass necessitates machining through the full thickness of the wafer, which is incompatible with most integrated electronic processes. MEMS inertial sensors with monolithically integrated electronics are commercially well established and are similar in structure to inertial energy harvesters, but they typically use surface-mounted proof masses of inadequate size for energy generation use. Furthermore, obtaining a substantial travel range with a monolithic device is difficult, as is a suspension that is highly flexible in the travel direction but effectively prevents motion in other axes.

Devices in which the proof mass is fixed using a stiff suspension form a mechanically resonant system. This is beneficial where the source motion amplitude is small, as it can provide resonant enhancement of the internal motion range, but has the important limitation of requiring excitation at or near a particular resonant frequency. This is particularly inappropriate for body-mounted energy harvesters, given the broad and varying spectrum of body motion. A possible solution to this problem is to actively tune the resonance frequency. Such tuning will typically require active control of the suspension stiffness; for example, in [10], a device is investigated in which permanent magnets provide additional stiffness that can be varied by adjusting the position of the magnets.

Manuscript received April 15, 2008; revised July 13, 2008. First published August 26, 2008; current version published April 1, 2009.

The authors are with the Optical and Semiconductor Devices Group, Department of Electrical and Electronic Engineering, Imperial College London, London, SW7 2BT, U.K. (e-mail: m.kiziroglou@ic.ac.uk).

Color versions of one or more of the figures in this paper are available online at http://ieeexplore.ieee.org.

Digital Object Identifier 10.1109/TIE.2008.2004381

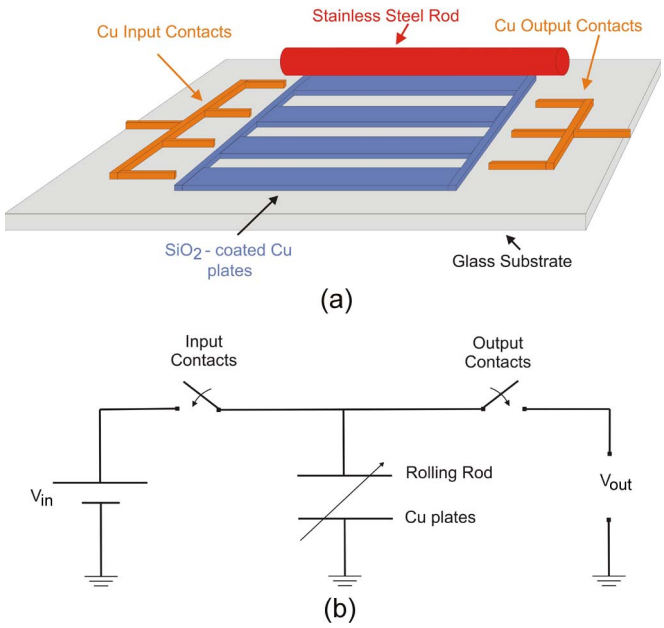

Fig. 1. (a) Schematic of the device structure. (b) Schematic circuit showing the electrical operation.

In this paper, a novel electrostatic energy harvester is described. An external free-rolling proof mass is used to address both the requirements for a large mass and broadband operation. All the other components are monolithically integrated with standard surface processing. We have previously presented this device concept in [11], but problems of inadequate surface flatness, low effective device capacitance, and excessive parasitic capacitance to the substrate meant that useful output power was not obtained. Here, we present a revised design and process flow, and show that output power is achieved.

II. Operating Principle

The operating principle is illustrated in Fig. 1. A series of strip electrodes forms the fixed plates of the variable capacitor and is covered by a thin dielectric layer. A metal cylinder forms the moving counter electrode. When the cylinder is aligned with one of the strip electrodes, it makes direct contact with an additional (narrow) charging contact, by which the necessary precharge is applied. This creates an electrostatic force between the cylinder and the strip electrode. Motion of the substrate then induces rolling of the cylinder, causing it to break contact with the precharge supply; the separation is then increased at constant charge, so that as the capacitance reduces, the stored energy increases due to the work done against the electrostatic force. The cylinder then makes contact with a discharge electrode, releasing this energy in the form of a high-voltage pulse. This operation is equivalent to that of the monolithic device of [7] but has the following key advantages: the mass can be significantly greater for an equivalent device size; no suspension structure is needed (although a guide structure will be required to constrain the motion); the travel range (to which the achievable power is also proportional) is greatly increased, partly because of the elimination of the flexural suspension; and the output is provided in several pulses per motion cycle rather than a single one. The latter characteristic is valuable because parasitic capacitances typically make it difficult to benefit from a large motion range in a single-pulse system.

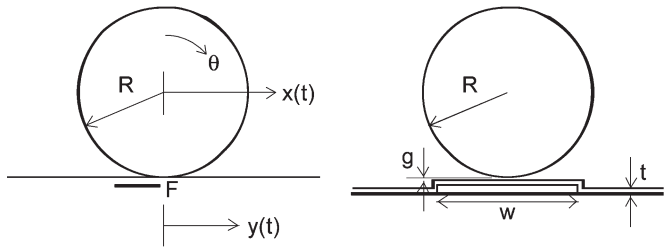

Fig. 2. Geometric notation for the dynamic motion analysis l and the device structure notation r.

III. Dynamic Analysis

The motion of the rod while the platform undergoes horizontal motion can be classified into slip and nonslip motions. The nonslip response can be analyzed using the notation of Fig. 2. We take $y(t)$ and $x(t)$ as the absolute positions of the platform and rod, respectively, with $z(t)$ as the relative motion, i.e., $z(t) = x(t) - y(t)$.

We can then write $z(t) = R\theta(t)$; thus,

$$\theta = \frac{x}{R} - \frac{y}{R}. \tag{1}$$

The platform motion will cause a force F to be applied on the rod at the point of contact, which accelerates the rod according to $F = m\ddot{x}$, with $\ddot{x}$ as the second time derivative of x. The force also results in a torque that rotates the rod according to $FR = I\ddot{\theta}$, with I as the moment of inertia. Taking the second derivative of (1) and equating $\ddot{\theta}$ gives

$$\frac{\ddot{x}}{R} - \frac{\ddot{y}}{R} = -\frac{m\ddot{x}R}{I} \tag{2}$$

which can be manipulated to give

$$\ddot{y} = \ddot{x}\left(1 + mR^2/I\right). \tag{3}$$

For a solid rod, $I = mR^2/2$. If we assume harmonic motion and integrate (3), we then get $x(t) = y(t)/3$, or equivalently,

$$z(t) = -\frac{2}{3}y(t). \tag{4}$$

This result is independent of frequency, indicating the broadband nature of the response. However, it shows that large source displacement amplitudes are needed to achieve the full internal travel range. Note that in this analysis, the electrostatic forces are not included, and these will tend to impede the relative motion; the full analysis is reported in detail for linear motion electrostatic devices in [9].

When sliding happens, the analysis becomes more complex. The condition for sliding to occur is when the maximum static friction is no longer able to provide enough acceleration to

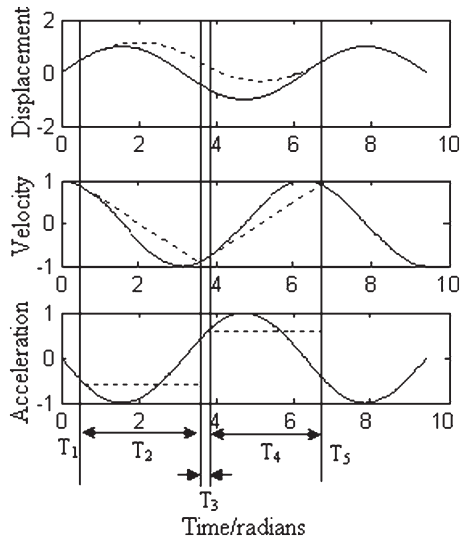

Fig. 3. Dynamic analysis of a rolling cylinder on a plain surface for (solid line) nonslip or (dashed line) slip motion.

synchronize the rod with the platform, i.e., for a harmonic source motion $y(t) = Y_\circ \cos(\omega t)$, sliding occurs if

$$\omega_0 \geq \sqrt{\frac{3\mu g}{Y_0}}. \tag{5}$$

A comparison between simulated nonslip and slip motions is shown in Fig. 3.

During T_1, the two motions coincide. At the start of T_2, the acceleration of the platform exceeds the condition in (5), and sliding starts. During this time, the acceleration of the rod will be constant because of constant sliding friction, velocity linearly varies because of constant acceleration, and displacement is quadratic. The two become in phase (no sliding) again when the velocity of the rod is the same as the platform, and the acceleration required at that time can be sufficiently provided by the static friction (T_3). At the end of T_3, the platform acceleration again exceeds friction's capability, and sliding starts. In T_4, the rod moves as in T_2 but in the opposite direction, and T_5 is a repetition of T_1. Considering the whole period, sliding occurs in T_2 and T_4; in other time slots, only rotation takes place.

IV. Simulations

The energy extracted per charge–discharge cycle in a constant-charge electrostatic generator is given by

$$\Delta U = \frac{1}{2}\frac{C_{\max}}{C_{\min}}(C_{\max} - C_{\min})V_i^2 \tag{6}$$

where $C_{\max}$ and $C_{\min}$ are the initial and final capacitances, and V_i is the priming voltage. Thus, it is important to maximize both the capacitance difference and the ratio, and since the minimum useable level will be limited by parasitics, maximizing $C_{\max}$ is crucial. The capacitance between a cylinder and a flat plane can analytically be solved. However, here, we have the added complications of a finite lower electrode width w, and a flat dielectric of thickness τ and relative permittivity ε_r, whereas the rest of the dielectric is air. There is also the possibility

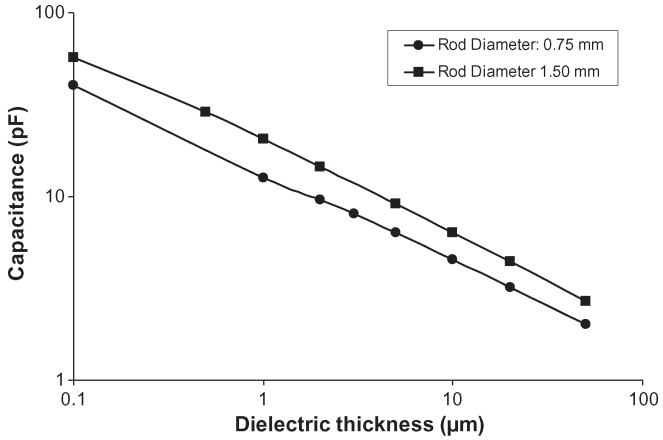

Fig. 4. Rod-to-plate capacitance versus dielectric thickness for two different rod diameters. The plate length was 10 mm, and the plate width was 1 mm.

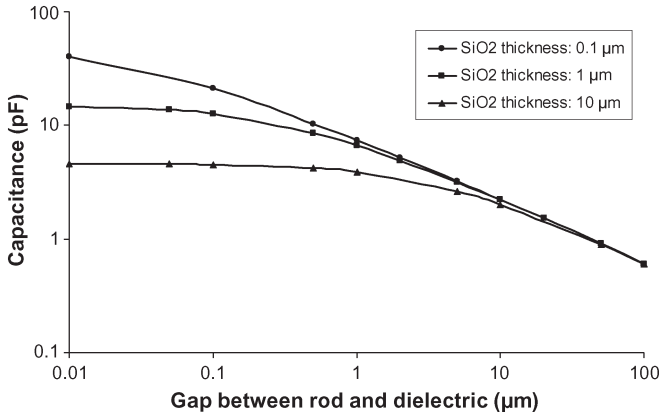

Fig. 5. Capacitance versus size of gap between the rod and the dielectric for different dielectric thicknesses. The plate length was 10 mm, and the plate width was 1 mm.

of a small air gap g between the rod and the dielectric film, for example, because of rod or substrate bow. Thus, we have used finite-element simulation to determine the capacitance. The results are shown in the following discussion.

Fig. 4 shows the capacitance versus dielectric thickness for different rod radii. Clearly, obtaining a low dielectric thickness is required, and this must be achieved over a significant surface area while avoiding pinholes that could lead to device shorting. We chose sputtered SiO_2 as our material because of its high deposited quality and stability, as well as good thickness control.

It is also possible that the rod does not achieve intimate contact with the dielectric layer, for example, because of surface roughness or curvature; thus, we have simulated the effect of a small air gap. The results (Fig. 5) indicate that the gap must be less than one tenth of the oxide thickness in order to have a negligible effect.

V. Fabrication

The wafer-lever fabrication process for the device is shown in Fig. 6.

A 4-in, 500-μm-thick Schott Borofloat33 glass wafer was used as the substrate; glass is used rather than Si in order to minimize parasitic capacitances. A 20-nm-thin Cr adhesion

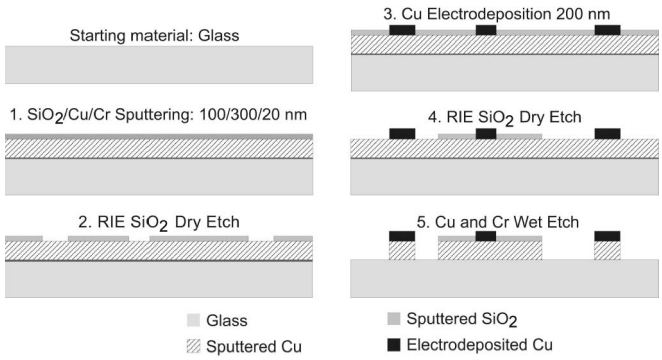

Fig. 6. Fabrication process flow for the substrate of the generator.

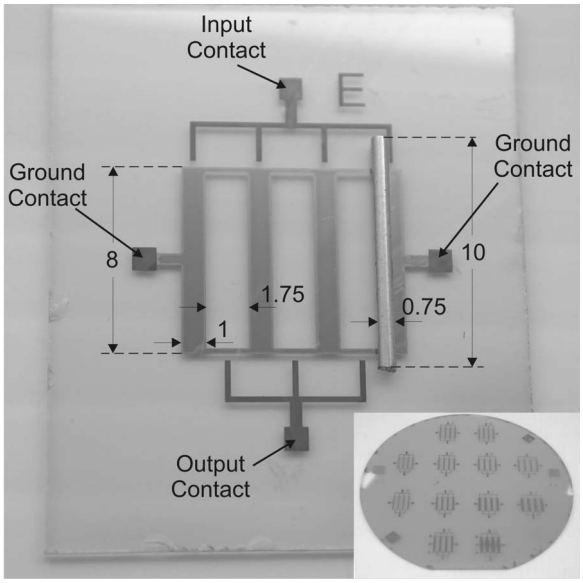

Fig. 7. Optical image of a fabricated harvesting device, including the stainless steel rod. The noted dimensions are in millimeters. A whole wafer of devices is shown in the inset.

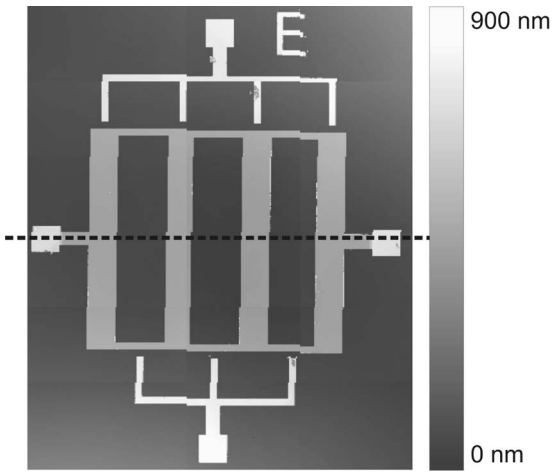

Fig. 8. Optical interferometry measurements.

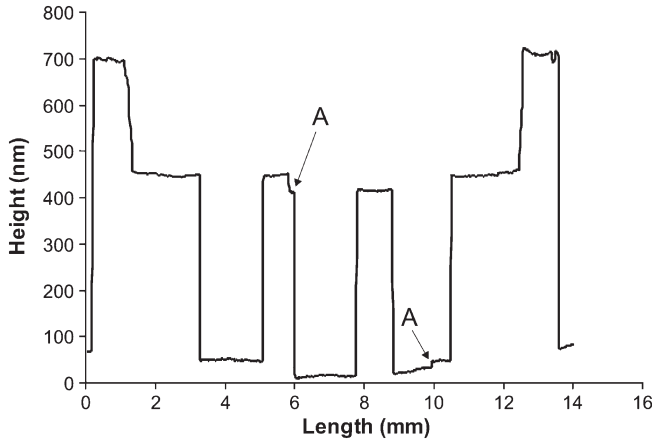

Fig. 9. Cross-sectional profile along the line indicated in Fig. 8. The plates and contact thicknesses are around 400 and 650 nm, respectively.

layer and a 300-nm Cu layer were sputtered on the glass wafer, followed by 100-nm SiO_2 sputtering (step 1 in Fig. 6). By conventional lithography, patterns of photoresist were defined on top, exposing only the contact areas of the devices. SiO_2 was etched at the contact areas using reactive-ion etching (RIE) (step 2), and Cu electrodeposition followed, to a thickness of 200 nm (step 3). This technique is promising for much finer calibration at the edge between SiO_2 and the Cu contact. Subsequently, the resist was stripped off the wafer, and a new resist pattern was defined to cover the plate and contact regions of the device. SiO_2 was etched using RIE (step 4), and Cu and Cr were etched using appropriate wet chemical etchants (step 5). A steel rod with a diameter of 0.75 mm was used for the proof mass.

An optical image of the device is shown in Fig. 7. The glass substrate with the Cu contacts and the SiO_2-covered Cu electrode strips is visible. The width of the strips is 1 mm, and the space between them is 1.75 mm. The length of the strips is 8 mm. A steel rod is also shown, with a diameter of 0.75 mm and a length of 10 mm. In the inset, a whole glass wafer of devices is illustrated.

VI. Characterization

A. Physical Characterization

Optical interferometry measurements were performed using a Zygo interferometer to accurately determine the physical dimensions of the device. A cross section of the device was extracted from the interferometry measurements along the dashed line of Fig. 8. The resulting profile is plotted in Fig. 9. The thicknesses of the SiO_2-covered plates and the contacts are 400 and 650 nm, respectively, giving a step of 250 nm. This step ensures that the rolling rod makes contact with the input and output pads as it rolls over the isolated plates. The steps marked as "A" in Fig. 9 are image artifacts resulting from stitching of subfields during interferometry scanning. The root-mean-square surface roughnesses of the sputtered SiO_2 and the electrodeposited Cu are both less than 10 nm. For these measurements, a square area with sides of 0.8 mm was used.

The corresponding surface profiles are shown in Fig. 10. These indicate a roughness amplitude of only a few nanometers.

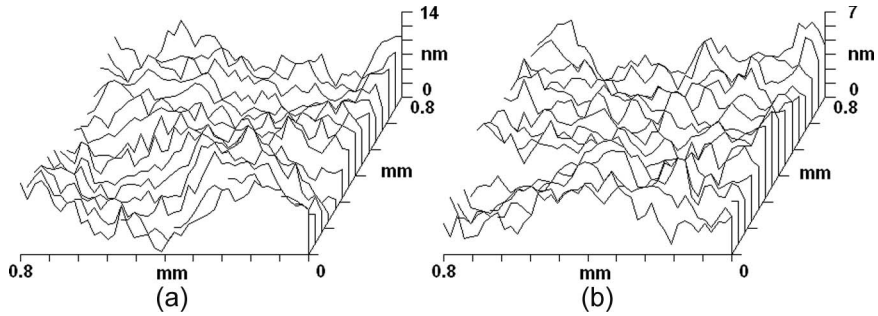

Fig. 10. Surface profiles for (a) sputtered SiO_2 and (b) electrodeposited Cu.

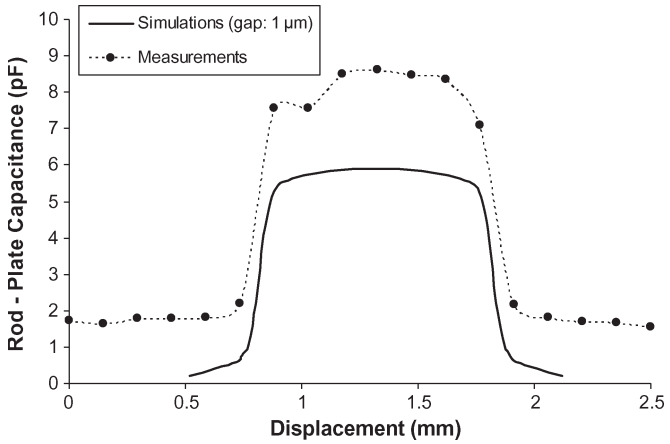

Fig. 11. Capacitance between the rod and the plate versus displacement as the rod rolls over one of the SiO_2-covered plates. The displacement is measured from the middle of the gap between two plates (see Fig. 7).

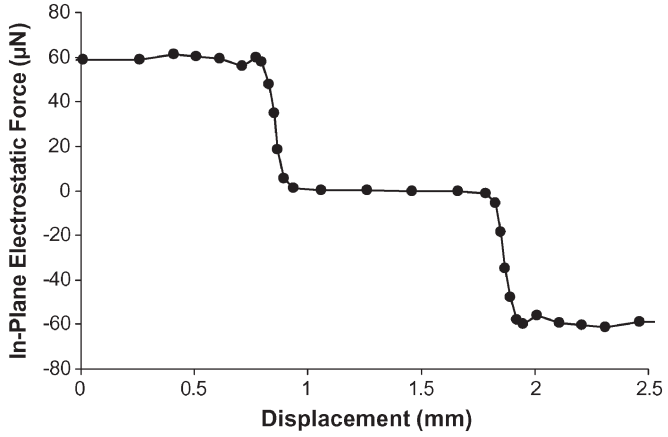

Fig. 12. Simulated electrostatic force between the rod and the plate versus displacement. The displacement is measured from the middle of the gap between two plates (see Fig. 7).

B. Capacitance Measurements

Among the most critical parameters for the successful operation of an electrostatic generator are the useful and parasitic capacitances throughout the device structure. The parasitic capacitances among the input contacts, the plates, and the output contacts were below the limits of detection of our apparatus at about 1.5 pF.

The capacitance between the steel rod and the plates was measured for different positions of the rod on the substrate along 1.25 mm from either side of the center of a substrate plate. During measurements, the rod was parallel to the long direction of the plates. The resulting values are plotted as black dots against displacement in Fig. 11. At the discharging position, a capacitance of around 2 pF is observed. As the rod reaches the left side of the plate, a sudden increase of the capacitance to around 8 pF is observed. The high capacitance value remains as long as the rod is above the plate. This corresponds to the charging position. When the rod rolls off the plate, the capacitance drops back to the value of around 2 pF.

Simulations of the capacitance against rod displacement of this geometry have been performed using the ANSYS software package. Assuming perfect contact of the rod to the dielectric, a rod-to-plate capacitance value of 40 pF is expected at the charging position for the geometric parameter values in this device. The difference between the measured and calculated rod-to-plate capacitances can be explained by taking into account the imperfection of the rod-to-dielectric contact. If an effective air gap of 1 μm is assumed, simulations give a capacitance of around 6 pF. The corresponding simulation results are shown as a solid line in Fig. 11.

The experimental behavior of capacitance versus lateral displacement matches the one predicted by the numerical simulations. The excess capacitance of around 2 pF observed throughout the displacement measurement range corresponds to the parasitic capacitance of the electrodes and measuring equipment. This matching indicates a 1-μm effective gap between the rod and the dielectric. This can be explained by taking into account the large length of the rod-to-substrate contact (10 mm), for which deviations on the micrometer scale can be explained by very modest bowing (1 μm corresponding to a radius of curvature of 10 m).

The in-plane electrostatic force applied on the rod can be written as a function of the stored charge Q, the capacitance C, and the capacitance gradient with respect to the displacement x, i.e.,

$$F = -\frac{dE_C}{dx} = \frac{Q^2}{2} \cdot \frac{1}{C^2} \cdot \frac{dC}{dx} \tag{7}$$

where E_C is the electrostatic energy stored in the device. The direction of the force is such that the rod is attracted toward alignment with the closest plate.

Using the simulation results of Fig. 11 for the rod-to-plate capacitance, the force as a function of displacement is calculated. The results are plotted in Fig. 12. While the rod is on the SiO_2-covered plate (displacement 1.25 $\pm$ 0.5 mm in Fig. 12), the

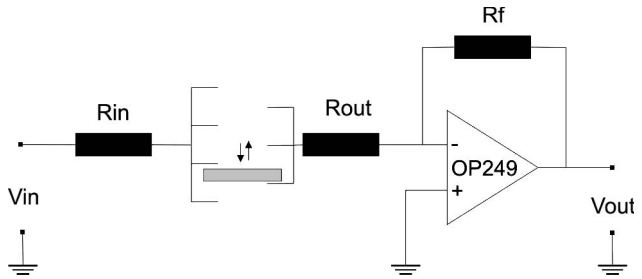

Fig. 13. Power generation measurement circuit.

in-plane force is negligible. As the rod rolls off the plate, there is a sharp increase of the absolute value of the force. Subsequently, as the rod rolls away from the plate, a constant electrostatic force is expected for distances up to 1 mm from the plate. At the discharge contacts, the charge is removed; thus, the force drops to zero until the rod reaches the next charging contact.

C. Output Voltage Measurements

The operation of the fabricated generator was tested by measuring the output voltage while a 0.75-mm-diameter rod was rolling over and in parallel with the plates. For testing, input (priming) voltages from 5 to 30 V were applied. In this paper, only results for 20 V are presented as they are indicative for the whole voltage range. It is noted that, as expected, a higher input voltage gives higher output voltage pulses.

Given the low value of the capacitance at the discharging position of the rod (less than 2 pF), a buffer circuit was used to provide high input resistance and low capacitance of the measuring system. The complete circuit is shown in Fig. 13. A resistor of $R_{\rm in} = 10$ kΩ is used at the input to prevent high current flow during any unwanted short-circuiting. At the output, a simple negative feedback operational amplifier (op-amp) configuration is used, with $R_{\rm out} = 10$ MΩ and $R_f = 1$ MΩ, corresponding to a gain of 0.1. The op-amp was an Analog Devices OP249, which was chosen for a high slew rate (22 V/μs) to meet the expected pulse characteristics. The voltage at the output of the buffering circuit was measured using a 10 : 1 probe and a digital oscilloscope.

A typical output pulse is shown in Fig. 14. A peak output voltage of 48 V is observed. This value corresponds to a voltage gain of 2.4, which is substantial but not optimal, as the capacitance measurements in Fig. 10 suggest an output-to-input voltage ratio of 4. This gain loss may be attributed to charge losses through SiO_2 during the rolling of the rod and to measurement-induced losses during pulse capturing by the buffering circuit.

Taking $C_{\rm min}$ as 2 pF, this corresponds to about 2 nJ per pulse, or 12 nJ for a full motion cycle with three charge–discharge cycles in each direction. Microwatt power levels are the likely minimum requirement for small electronic devices such as sensors; for input frequencies above 100 Hz (e.g., machine motion), this is already achievable at such output levels, but more than an order of magnitude increase will be needed for body motion applications where the frequencies are a few hertz or less. This will require higher capacitance values $C_{\rm max}$ and

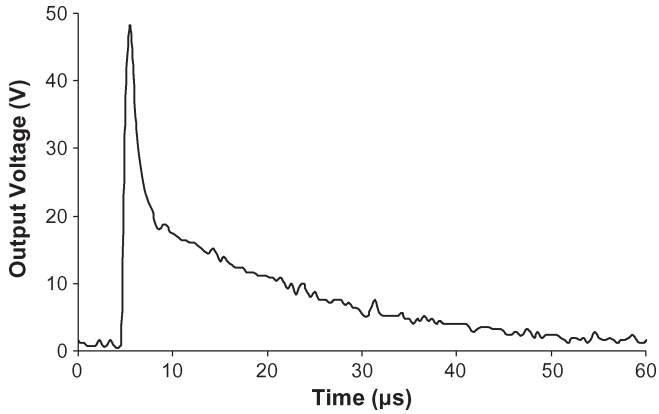

Fig. 14. Typical output voltage pulse of the electrostatic generator.

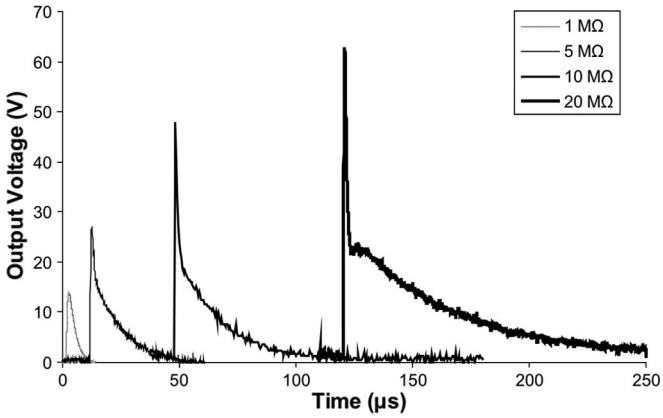

Fig. 15. Output voltage pulses of the generator for an input voltage of 20 V and for different values of the measuring circuit input resistance $R_{\rm in}$.

TABLE I
OUTPUT DISCHARGE TIME CONSTANTS

R_{out} (MΩ)	Short discharging RC (μs)	Long discharging RC (μs)
1	4	4
5	4	11
10	4	22
20	3	51

$C_{\rm min}$ if significantly increased input and output voltage levels are to be avoided.

During measurements, the produced output power is stored as charge at the rod–plate capacitor. The discharge time is much shorter than the duration of contact between the rod and the output pad (>1 ms) [12]. Two discharge regions with different time constants are visible in Fig. 14. In order to investigate the origin of these two discharge mechanisms, output measurements for different values of the resistor $R_{\rm out}$ were performed. The results are shown in Fig. 15. The time constants for both discharge regions were extracted from such pulses and are presented in Table I.

The short discharging time constant is independent of $R_{\rm out}$ and can be explained as charge sharing with the parasitic capacitance between the discharge contacts and earth at the moment of contact. The level of voltage drop between the peak and the commencement of the slow discharge, typically about

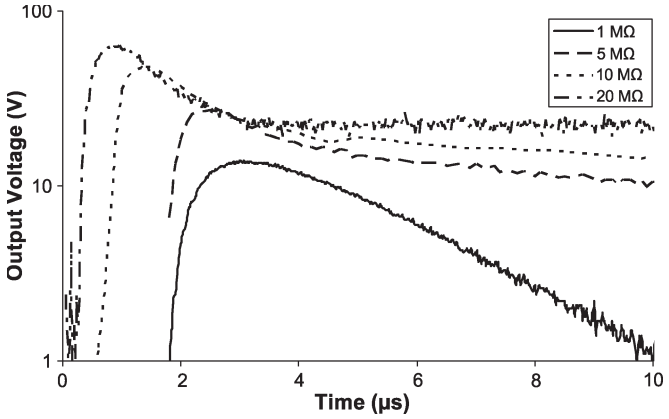

Fig. 16. Output voltage pulses of Fig. 15 replotted on a logarithmic scale.

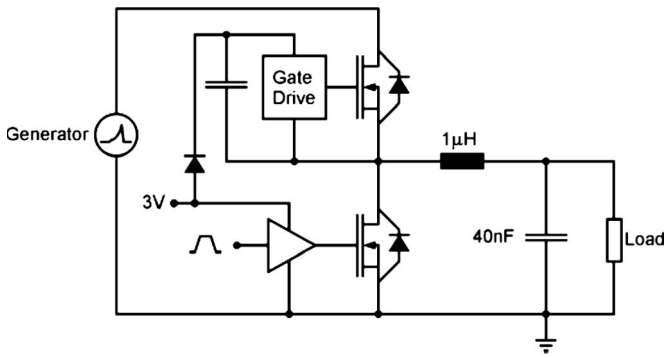

Fig. 17. Half-bridge step-down power converter based on [12].

half the peak, suggests a magnitude of parasitic capacitance on the order of $C_{\min}$, i.e., a few picofarads. This charge-sharing effect should be nearly instantaneous, and the observed rise and fall times are thus limited by the speed of the op-amp circuit. On the other hand, the longer discharge time is approximately proportional to $R_{\text{out}} + R_f$ and, thus, corresponds well to the discharge of $C_{\min}$ into the output of the op-amp for a discharge capacitance value of 3 ± 1 pF. This can be more clearly seen in Fig. 16, where the discharge waveforms are plotted on a logarithmic scale. The results are in agreement with the capacitance measurements presented in Fig. 10, showing a capacitance of 2 pF at the output position.

In common with previous electrostatic generators, the device reported here provides power in short output pulses. These pulses need to be efficiently transformed to a usable form, i.e., a dc voltage. This requirement has been addressed in detail for parallel-plate constant-charge energy harvesters [12], and the results are equally applicable here. A suitable conversion/regulation circuit using a half-bridge step-down power converter is shown in Fig. 17.

The electrostatic generator for which this converter was designed [7] produced very high output pulse voltages (>100 V). Consequently, a novel metal–oxide–semiconductor field-effect transistor design was required for the switching transistors in the circuit in order to provide the unusual combination of requirements, i.e., a high blocking voltage, a low channel resistance, and a low input capacitance. In contrast, the present device somewhat relaxes these requirements, as the distribution of the output power of one period of rod motion to a number of output pulses reduces the output amplitudes. This difference may simplify the design and fabrication of the power converter required for the commercial application of the rolling rod electrostatic microgenerator.

VII. Conclusion

In this paper, a novel implementation of the recently proposed rolling rod electrostatic microgenerator has been presented, and successful operation of the device has been demonstrated. The experimental results were compared with simulations, and it was shown that the increase of capacitance, and hence power generation, is possible by reducing the air gap between the rod and the dielectric.

Significant further development is required for the application of this MEMS energy-harvesting device. Higher capacitance values must be achieved through reduced dielectric thickness and improved rod–surface contact precision to increase the energy per pulse. Power conversion circuits satisfying the requirements of high voltage handling, high efficiency, and minimal parasitics must be integrated with the device. A packaging solution is needed, which can constrain the rolling proof mass in its correct trajectory without impeding its motion. However, the feasibility of this novel device concept has been demonstrated and offers the potential for a MEMS scale motion energy harvester, along with the ability to achieve substantial proof mass size and displacement range without the high-cost processes of through-wafer machining, or integrated suspensions.

References

[1] J. A. Paradiso and T. Starner, "Energy scavenging for mobile and wireless electronics," *Pervasive Comput.*, vol. 4, no. 1, pp. 18–27, Jan.–Mar. 2005.

[2] S. Roundy, P. K. Wright, and J. M. Rabaey, *Energy Scavenging for Wireless Sensor Networks*, 1st ed. Boston, MA: Kluwer, 2003.

[3] P. D. Micheson, T. Sterken, C. He, M. E. Kiziroglou, E. M. Yeatman, and R. Puers, "Electrostatic microgenerators," *Meas. Control*, vol. 41, no. 4, pp. 114–119, 2008.

[4] S. Meninger, J. O. Mur-Miranda, R. Amirtharajah, A. P. Chandrakasan, and J. H. Lang, "Vibration-to-electric energy conversion," *IEEE Trans. Very Large Scale Integr. (VLSI) Syst.*, vol. 9, no. 1, pp. 64–76, Feb. 2001.

[5] S. Roundy, P. K. Wright, and K. S. Pister, "Micro-electrostatic vibration-to-electricity converters," in *Proc. ASME Int. Mech. Eng. Congr. Expo.*, New Orleans, LA, Nov. 2002, pp. 1–10.

[6] T. Sterken, P. Fiorini, K. Baert, R. Puers, and G. Borghs, "An electret-based electrostatic μ-generator," in *Proc. 12th Int. Conf. Solid State Sensors, Actuators Microsyst. (TRANSDUCERS)*, Boston, MA, Jun. 2003, pp. 1291–1294.

[7] P. Miao, P. D. Mitcheson, A. S. Holmes, E. M. Yeatman, T. C. Green, and B. H. Stark, "MEMS inertial power generators for biomedical applications," *Microsyst. Technol.*, vol. 12, no. 10, pp. 1079–1083, Aug. 2006.

[8] B. C. Yen and J. H. Lang, "A variable-capacitance vibration-to-electric energy harvester," *IEEE Trans. Circuits Syst. I, Reg. Papers*, vol. 53, no. 2, pp. 288–295, Feb. 2006.

[9] P. D. Mitcheson, T. C. Green, E. M. Yeatman, and A. S. Holmes, "Architectures for vibration-driven micropower generators," *J. Microelectromech. Syst.*, vol. 13, no. 3, pp. 429–440, Jun. 2004.

[10] V. R. Challa, M. G. Prasad, Y. Shi, and F. T. Fisher, "A vibration energy harvesting device with bidirectional resonance frequency tunability," *Smart Mater. Struct.*, vol. 17, no. 1, p. 015 035, Feb. 2008.

[11] M. E. Kiziroglou, C. He, and E. M. Yeatman, "Electrostatic energy harvester with external proof mass," in *Proc. Power MEMS*, Freiburg, Germany, Nov. 28–29, 2007, p. 117.

[12] B. H. Stark, P. D. Mitcheson, P. Miao, T. C. Green, E. M. Yeatman, and A. S. Holmes, "Power processing issues for micro-power electrostatic generators," in *Proc. 35th Annu. IEEE Power Electron. Spec. Conf.*, Aachen, Germany, 2004, pp. 4156–4162.

Michail E. Kiziroglou (M'04) received the Diploma in electrical and computer engineering from Aristotle University of Thessaloniki, Thessaloniki, Greece, in 2000, the M.Sc. degree in microelectronics and nanoelectronics from Democritus University of Thrace, Xanthi, Greece, in 2003, and the Ph.D. degree in microelectronics and spintronics from the University of Southampton, Southampton, U.K., in 2007.

He is currently a Researcher with the Optical and Semiconductor Devices Group, Department of Electrical and Electronic Engineering, Imperial College London, London, U.K. His research interests include novel microelectromechanical systems, semiconductor integration, and nanoelectronic devices.

Cairan He received the B.S. degree in 2006 from Imperial College London, London, U.K., where he is currently working toward the Ph.D. degree in the Optical and Semiconductor Devices Group, Department of Electrical and Electronic Engineering.

His research interests include microelectromechanical systems and energy scavenging for wireless sensor nodes.

Eric M. Yeatman (M'01–SM'05) received the B.Sc. degree from Dalhousie University, Halifax, NS, Canada, in 1983, and the Ph.D. degree from Imperial College London, London, U.K., in 1989.

Since 1989, he has been a Member of Academic Staff in the Optical and Semiconductor Devices Group, Department of Electrical and Electronic Engineering, Imperial College London, where he is currently a Professor of microengineering and the Deputy Head of the group. His research interests include micromechanical actuators and generators, microstructures for optical and radio frequency applications, and technologies for pervasive sensing.